Supporting Information

Xuezhong Zhang[1,2], Die Wu[1, 4], Hongju Zhou[3], Dong Xiang[2], Haoming Sun[2], Chuanliang Chen[1], Dong Li[2], Yuanpeng Wu[2], Qiang Fu[1], Hua Deng[1*]

1. College of Polymer Science and Engineering, State Key Laboratory of Polymer Materials Engineering, Sichuan University, Chengdu 610065, PR China

2. School of New Energy and Materials, Southwest Petroleum University, Chengdu 610500, PR China

3. Department of Nephrology, Kidney Research Institute, West China Hospital, Sichuan University, Chengdu 610041, China

4. Institute for Mathematical and Computational Materials Science, Chengdu Advanced Metal Materials Industry Technology Research Institute Co., Ltd., Chengdu 610300, Sichuan, China

Corresponding author: huadeng@scu.edu.cn (H. Deng)

1. Experimental

1.1. Fabrication of AgNW@ANF and CS dendritic particle

Firstly, ANF/DMSO solution (0.5 wt%) was slowly dropped into the highly turbulent flow of IPA, which was formed by high-speed shearing of IPA by the IKA Magic Lab device (IKA Works Inc.) operating at 20000 rpm. Subsequently, AgNWs were dispersed in ANF dendritic particle with different ratios by alternately performing bath sonication (300 W, 10 min) and magnetic stirring (400 rpm, 2 h) to prepare AgNW@ANF dendritic particles. Finally, the IPA was sheared at 20000 rpm, and the CS aqueous solution (1.0 wt %) was slowly added with high turbulence to obtain CS dendritic particles.

1.2. Fabrication of AgNW@ANF film

AgNW@ANF films were obtained by suction filtration and drying at 60 °C for 5 h using AgNW@ANF dendritic particles.

1.3. Fabrication of AgNW@ANF/CS film

First, CS dendritic particles were filtered by vacuum-assisted suction. Following this process, the solvent from AgNW@ANF dendritic particles was removed using vacuum-assisted suction filtration. Finally, AgNW@ANF/CS films were obtained by repeating the above procedure and drying the material at 60°C for 5 hours.

1.4. Fabrication of AgNW@ANF/CS-C film

First, CS dendritic particles were filtered by vacuum-assisted suction. Following this process, the solvent from AgNW@ANF dendritic particles was removed using vacuum-assisted suction filtration. Finally, AgNW@ANF/CS-C films were obtained by repeating the above procedure and soaking in a glyoxal aqueous solution at pH 3.0 for 12 h and drying the material at 60°C for 5 hours.

1.5. Fabrication of AgNW@ANF/CS-CH film

Firstly, AgNW@ANF films were obtained by suction filtration and drying at 60 °C for 5 h using AgNW@ANF dendritic particles. Next, AgNW@ANF/CS films were fabricated by suction filtration and dried at 60°C for 5 h using AgNW@ANF and CS dendritic particles. Subsequently, AgNW@ANF/CS film was immersed in a glyoxal aqueous solution at pH 3.0 for 12 h and dried at 60 °C for 5 h to prepare AgNW@ANF/CS-C film. Finally, AgNW@ANF/CS-CH films were prepared by hot pressing sintering of AgNW@ANF/CS-C under 200 °C and 30 MPa for 30 min.
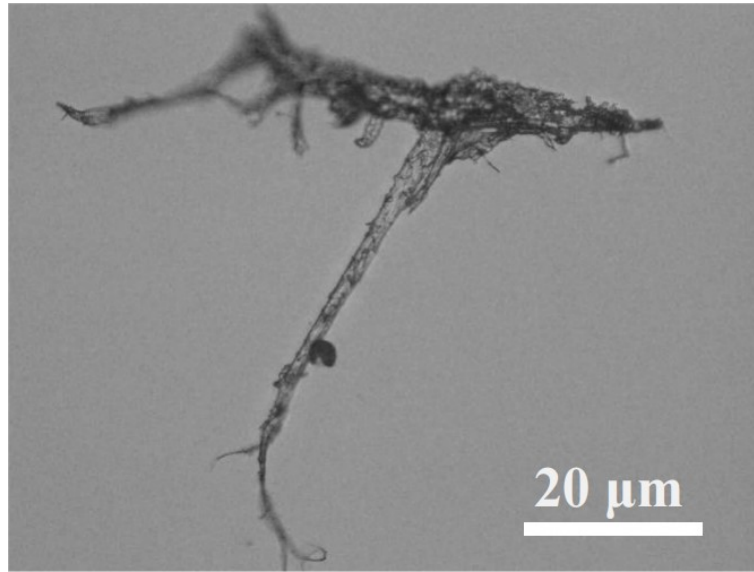
2. Characterization of materials

Fig. S1. Digital phoσtographs of CS dendritic particles.
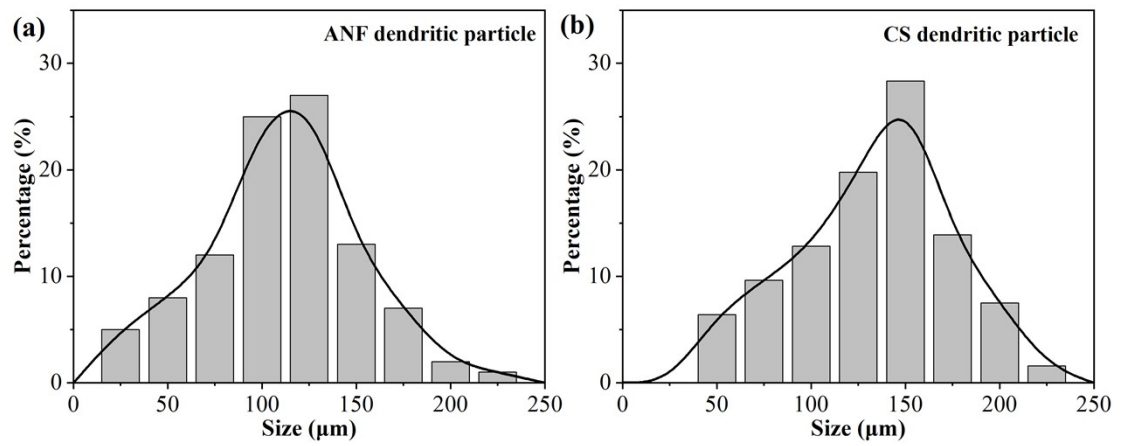

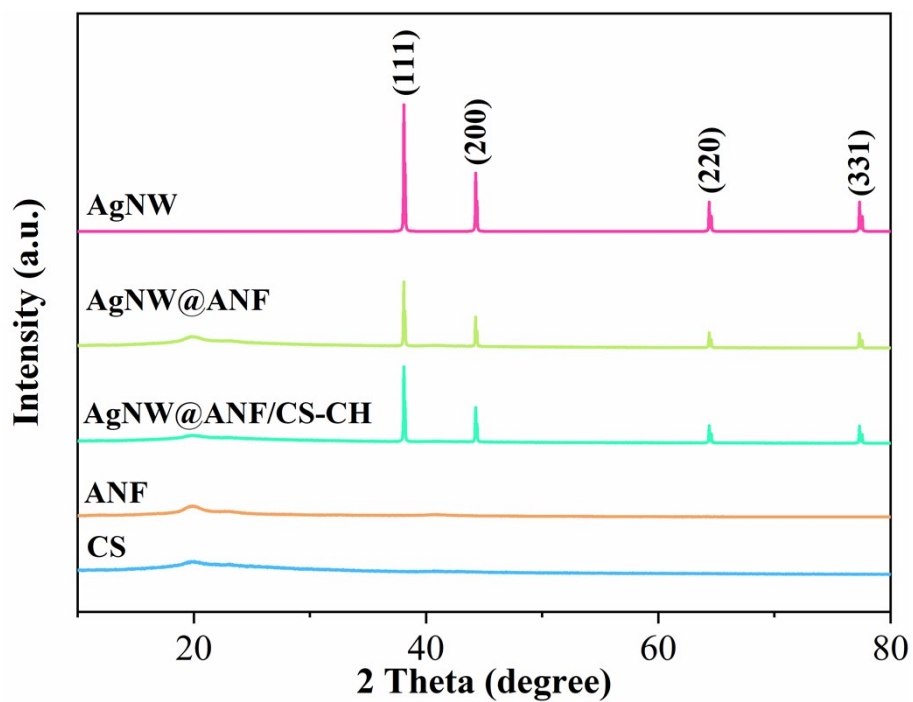**Fig. S2.** Size distribution of ANF and CS dendritic particles.

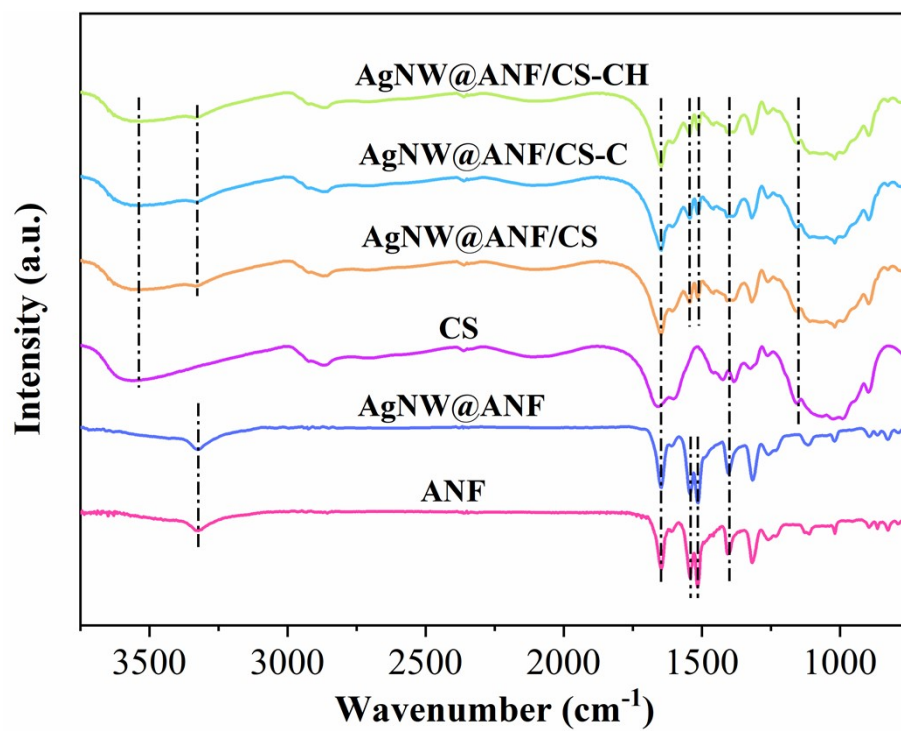**Fig. S3.** XRD of AgNW, ANF, CS, AgNW@ANF and AgNW@ANF/CS-CH.

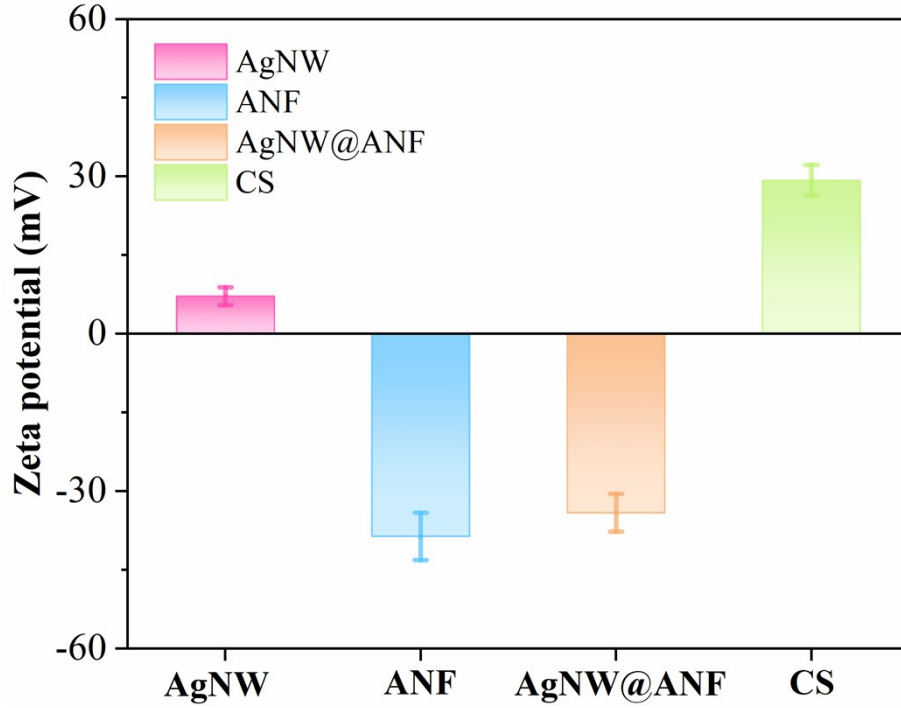**Fig. S4.** FTIR of ANF, CS, AgNW@ANF and AgNW@ANF/CS-CH.

Fig. S5. Zeta potential of AgNW, ANF, AgNW@ANF and CS dendritic particles.

2.1. Calculation of porosity

The theoretical volume is calculated according to the ratio between different components, the density and weight of these specimens, and then the actual volume is measured to compare to the theoretical volume to obtain the porosity. The porosity of film is estimated according to Eq. S1:

$$P\,(\%) = (1 - \frac{m_{AgNW}/\rho_{AgNW} + m_{ANF}/\rho_{ANF} + m_{CS}/\rho_{CS}}{\pi r^2 t}) \qquad \textbf{\textit{Eq. S1}}$$

Where m_{AgNW}, m_{ANF} and m_{CS} represents the weight of AgNWs, ANF and CS, respectively. ρ_{AgNW}, ρ_{ANF} and ρ_{CS} is the density of AgNWs, ANF and CS, respectively. r is the radius of the samples and t represents the thickness[1].
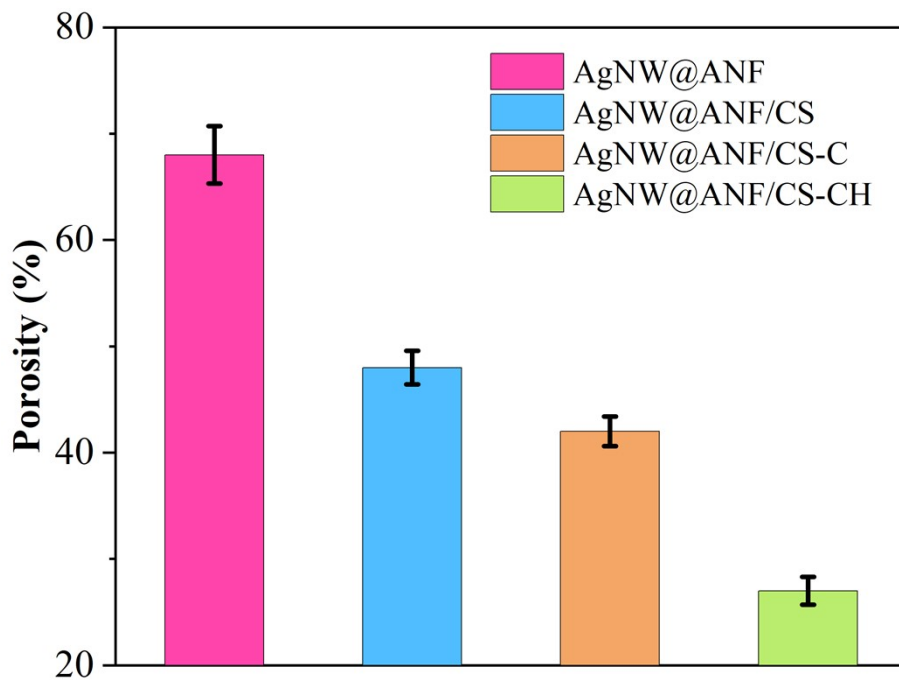
Fig. S6 Porpsity of AgNW@ANF, AgNW@ANF/CS, AgNW@ANF/CS-C and AgNW@ANF/CS-CH film.

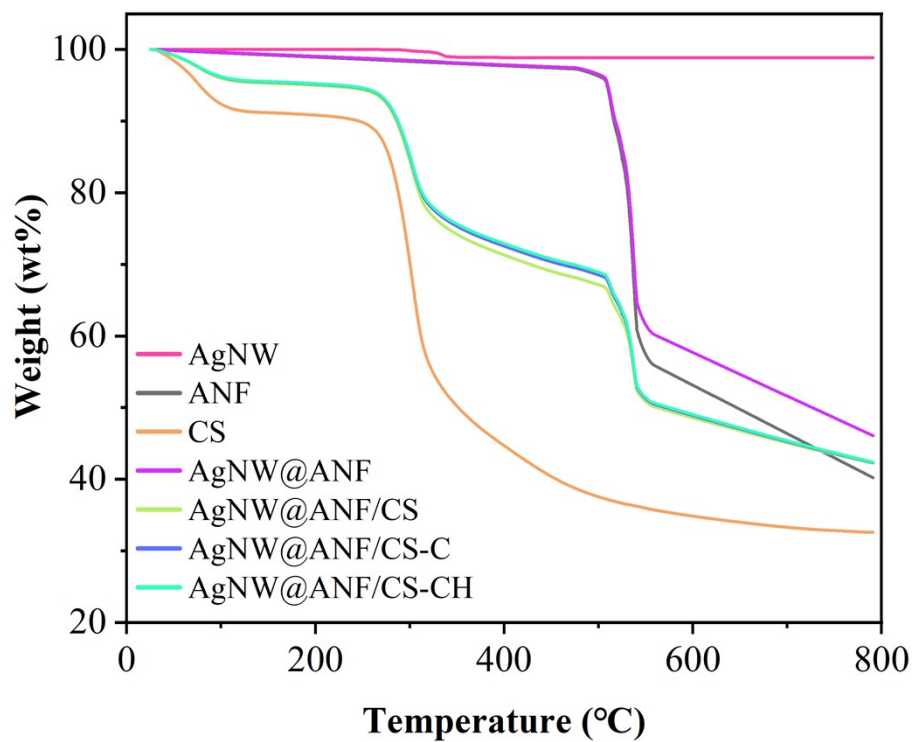## 2.2. Thermal gravimetric analysis (TGA)

Fig. S7. TGA of AgNW, ANF, CS, AgNW@ANF, AgNW@ANF/CS, AgNW@ANF/CS-C and AgNW@ANF/CS-CH film.
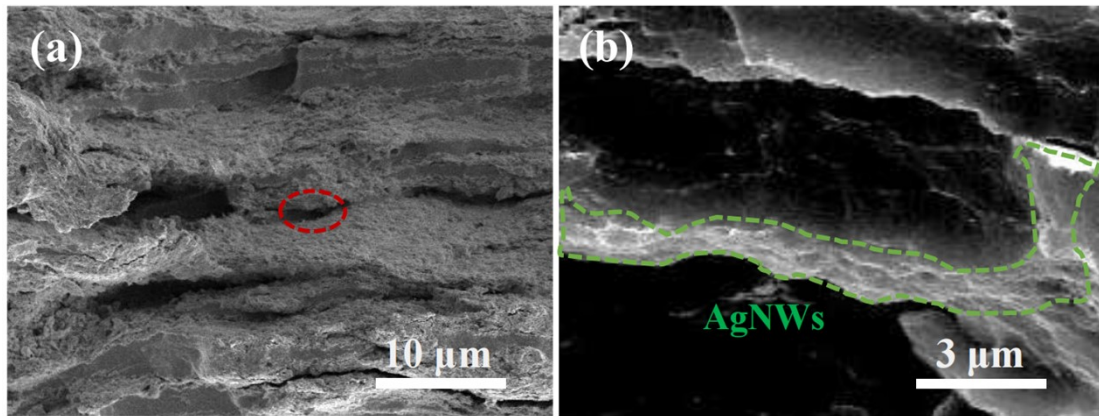
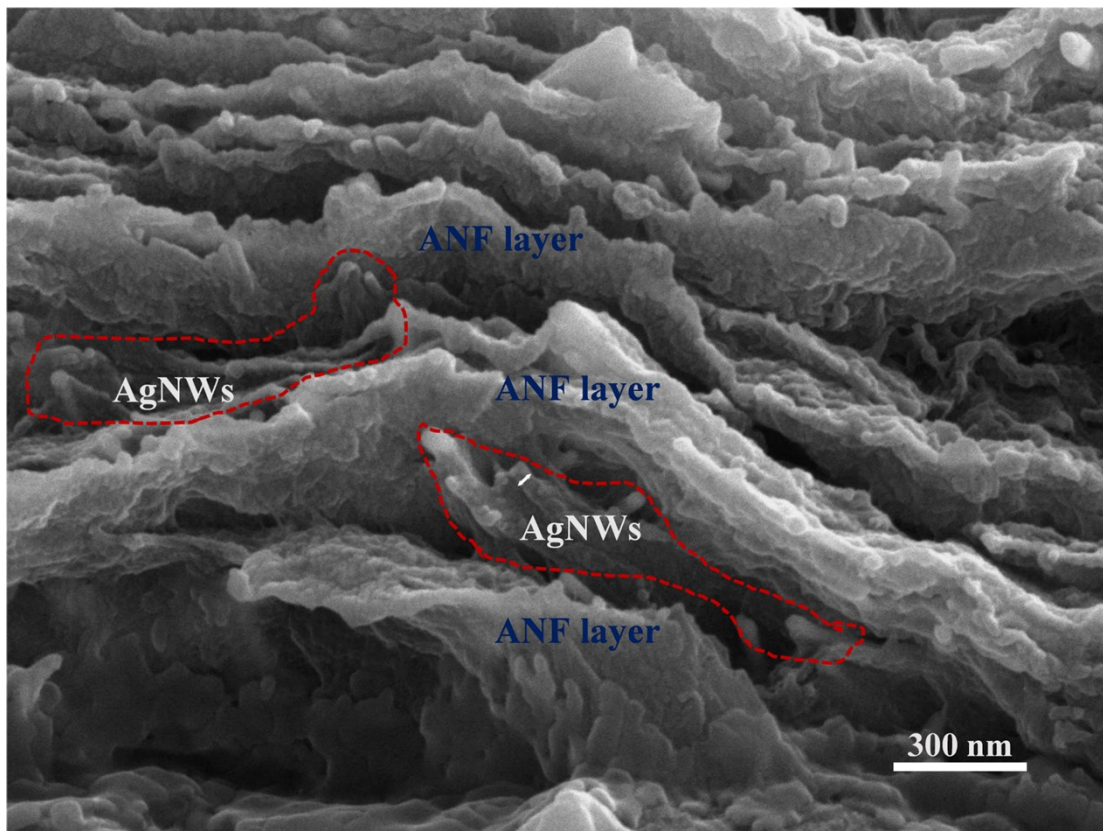**Fig. S8.** SEM of AgNW@ANF/CS-CH film in Y-axis direction

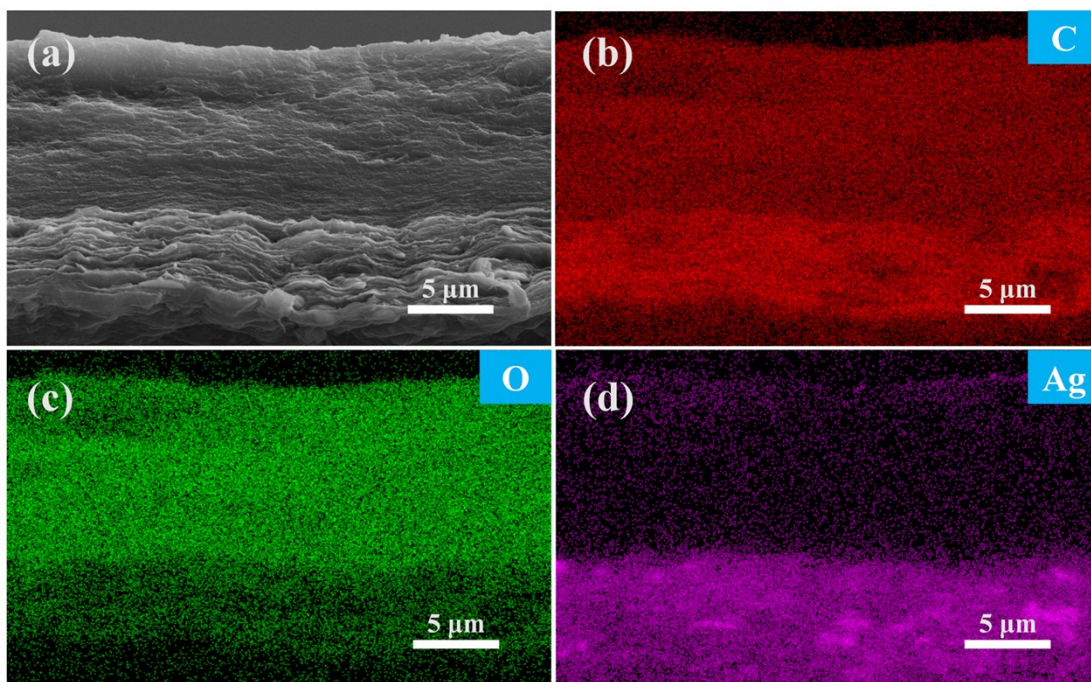**Fig. S9.** SEM of AgNW@ANF/CS-CH film cross-section at high magnification

Fig. S10. EDS of AgNW@ANF/CS-CH film
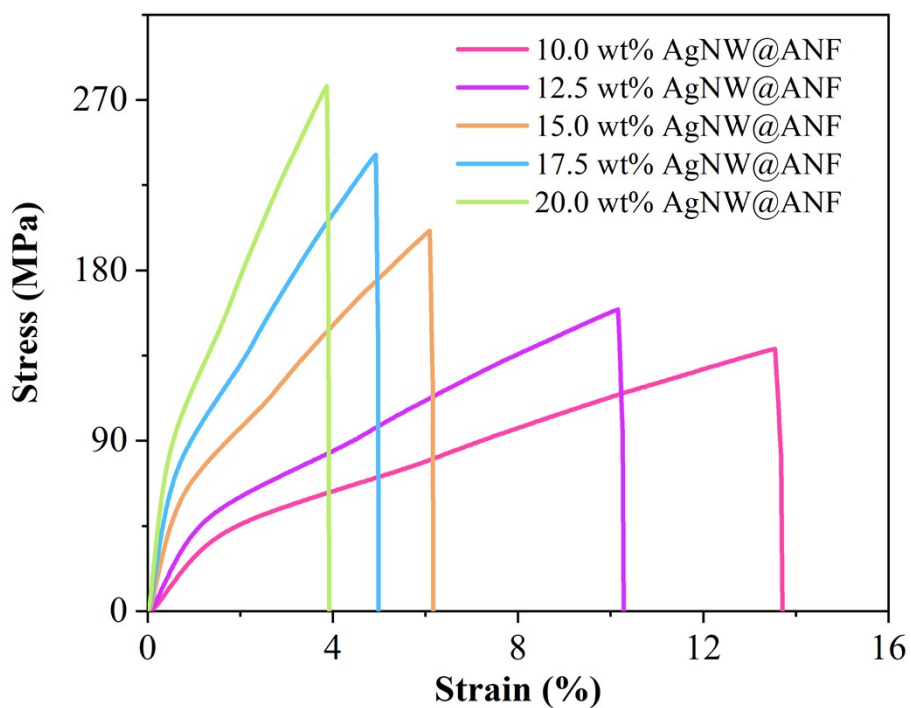
3. Mechanical Properties

Fig. S11. Stress-strain curves of AgNW@ANF films with different AgNW content.
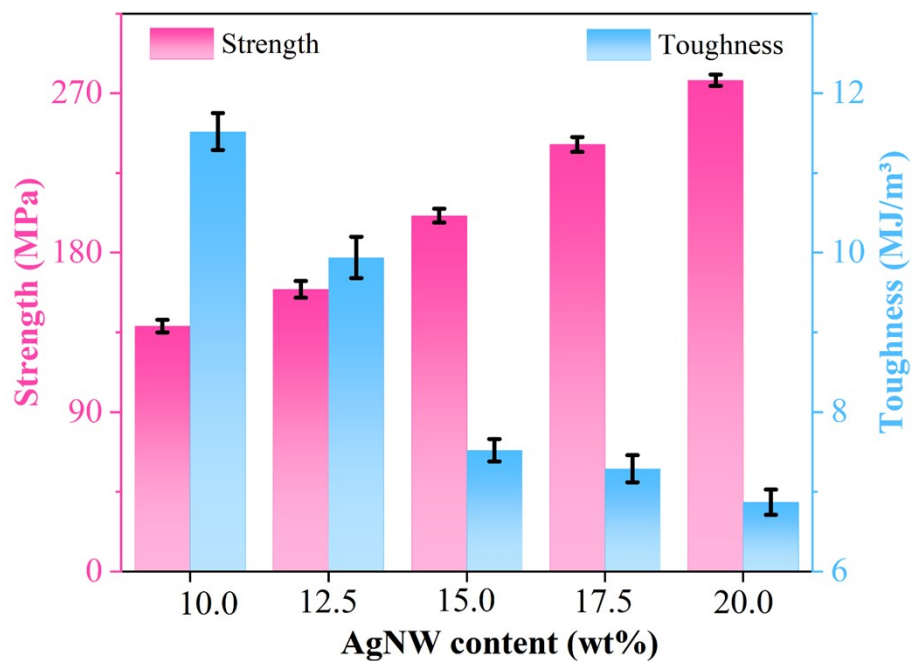
Fig. S12. Strength and toughness of AgNW@ANF film with different AgNW content.
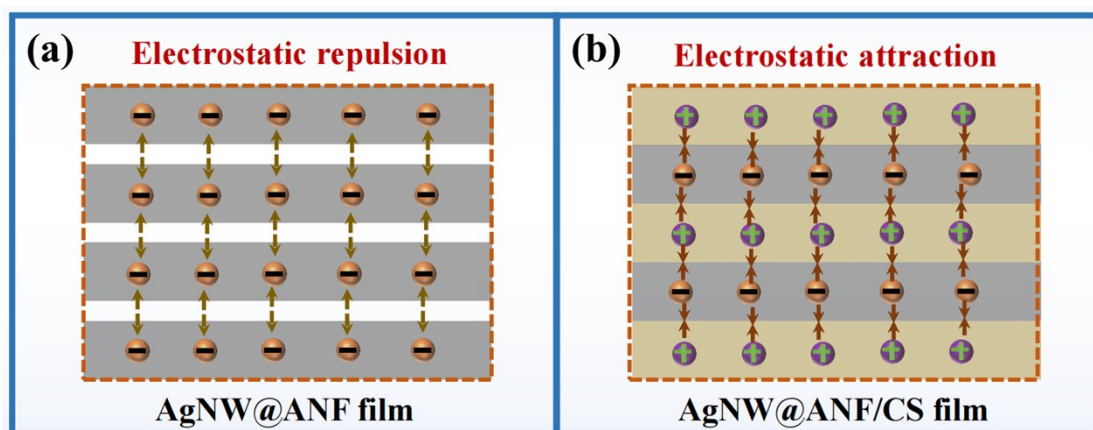

Fig. S13. The mechanism diagram of electrostatic electrostatic assembly: (a) AgNW@ANF and (b) AgNW@ANF/CS film.
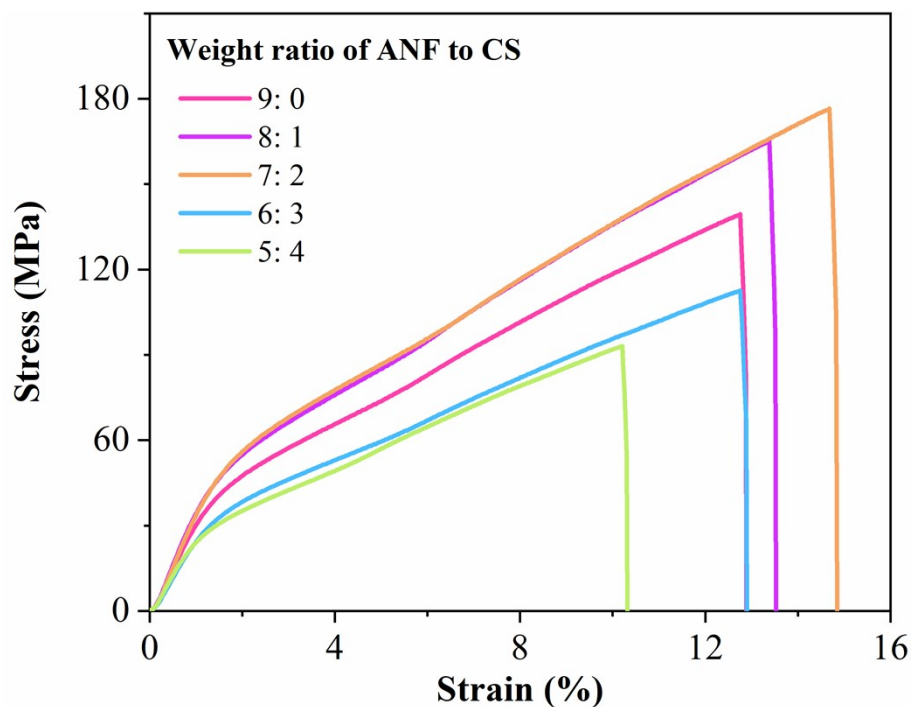
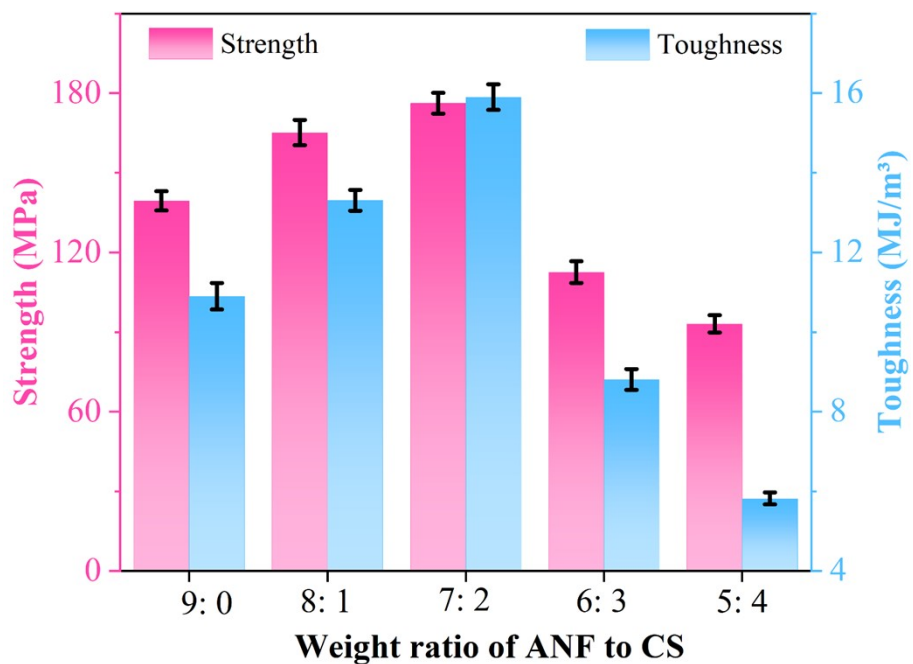**Fig. S14.** Stress-strain curves of AgNW@ANF films with different ANF and CS ratios.

Fig. S15. Strength and toughness of AgNW@ANF film with different ANF and CS ratios.
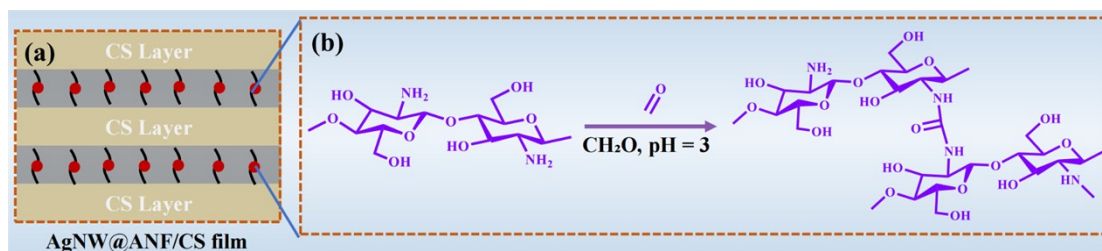

Fig. S16. Crosslinking of AgNW@ANF/CS-C film: (a) schematic and (b) mechanism diagram.

Fig. S17. Stress-strain curves of AgNW@ANF/CS-C films under different crosslinking agents.

Fig. S18. Stress and elongation of the films under different crosslinking agents.
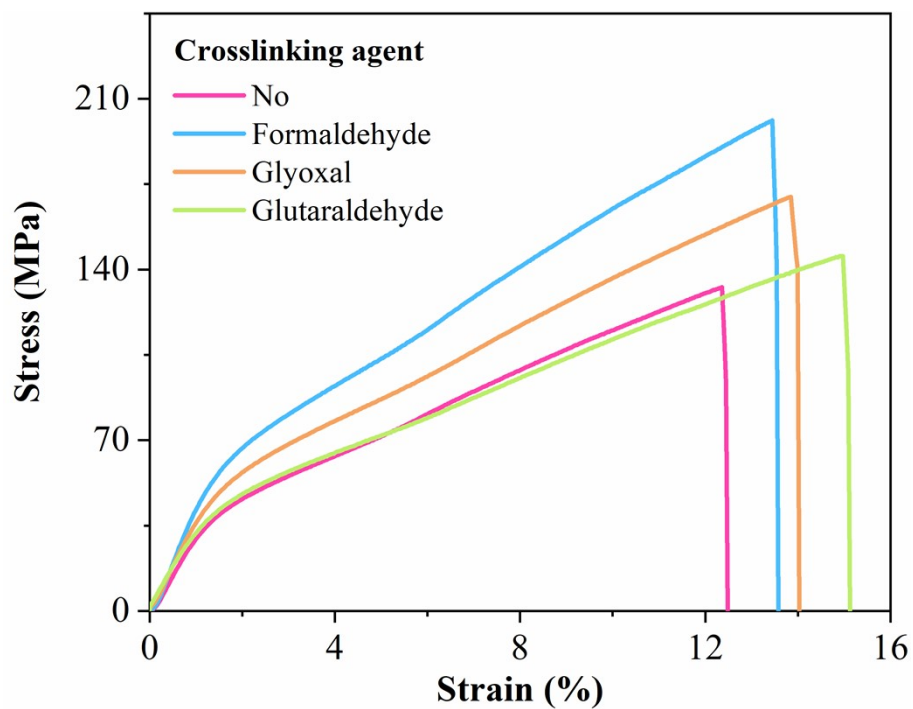
Fig. S19. Stress-strain curves of AgNW@ANF/CS-C films under different crosslinking pH.
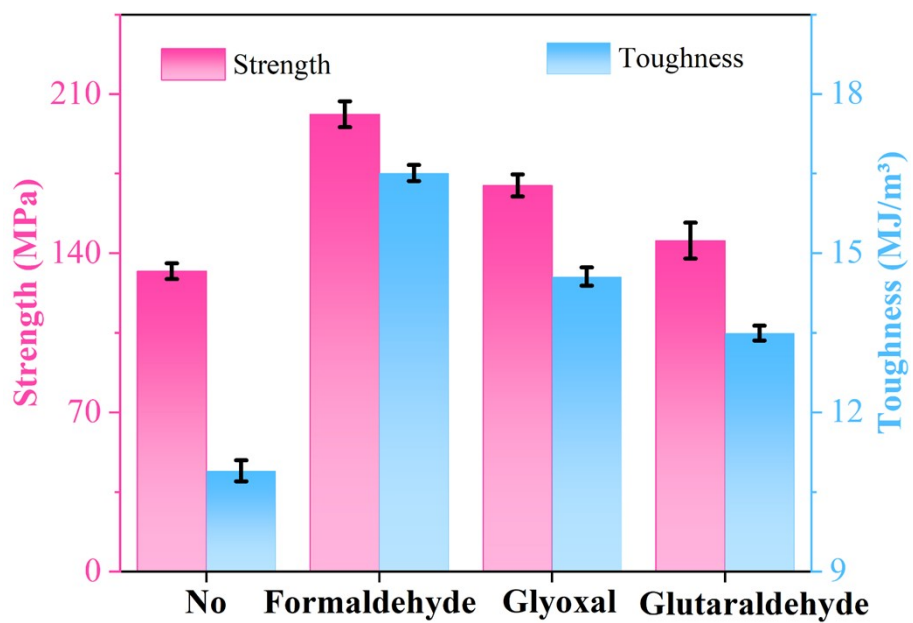

Fig. S20. Stress and elongation of the films under different crosslinking pH.

Fig. S21. Stress-strain curves of AgNW@ANF/CS-C films under different sintering pressure.
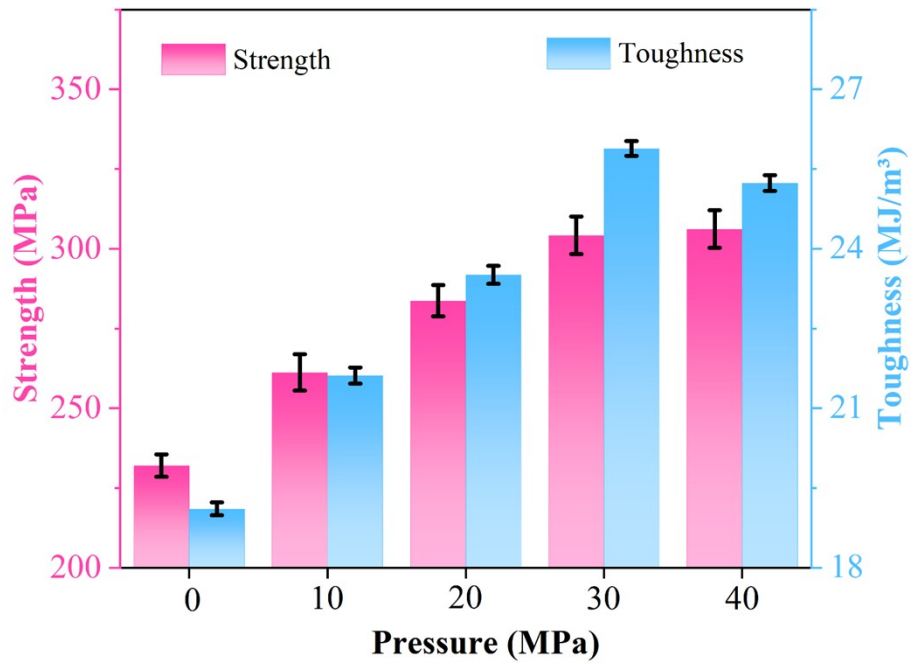
Fig. S22. Stress and elongation of the films under different sintering pressure.

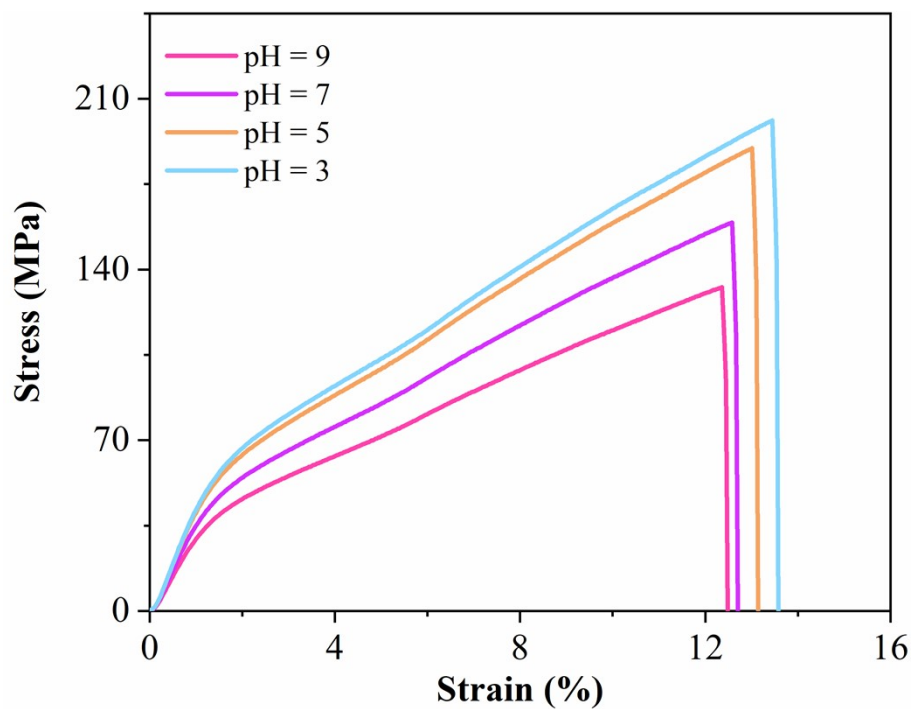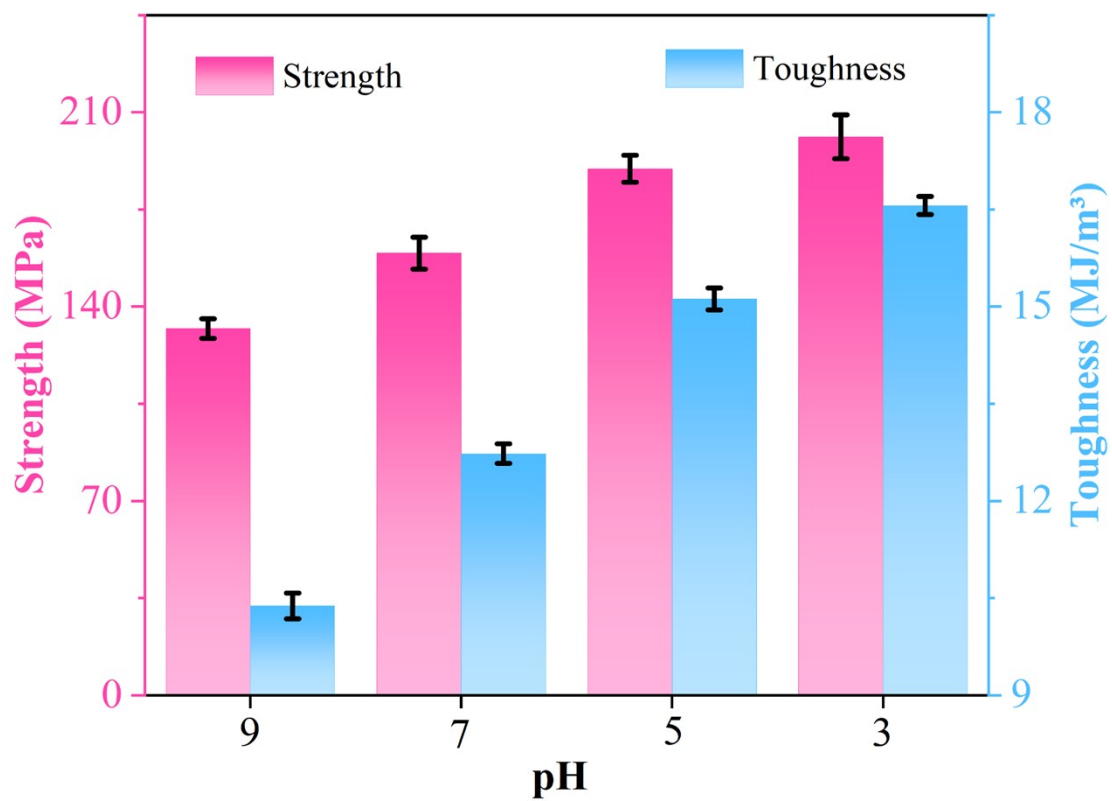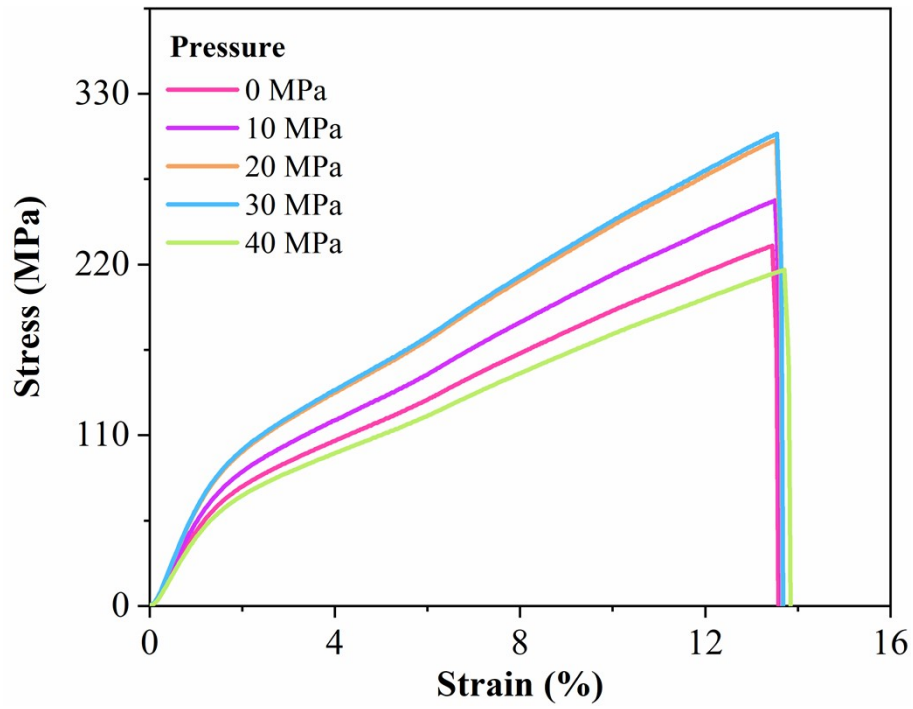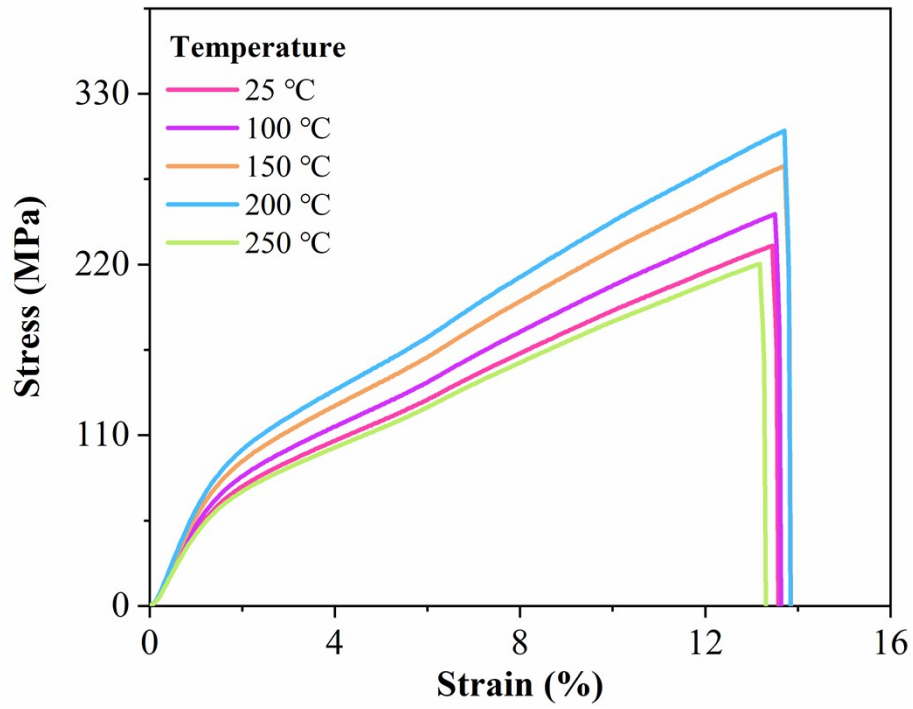**Fig. S23.** Stress-strain curves of AgNW@ANF/CS-C films under different sintering temperatures.
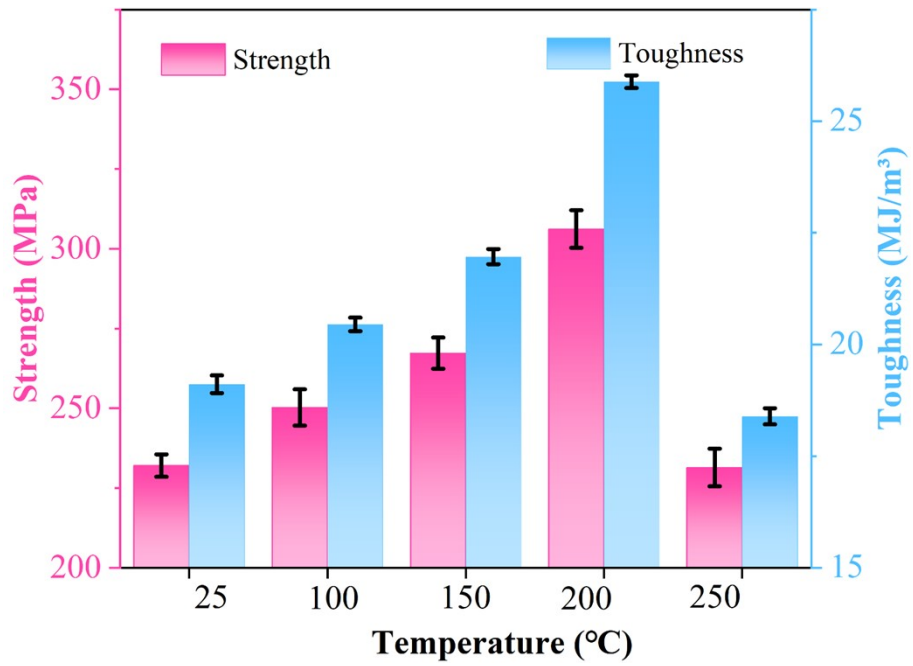
Fig. S24. Stress and elongation of the films under different sintering temperatures.
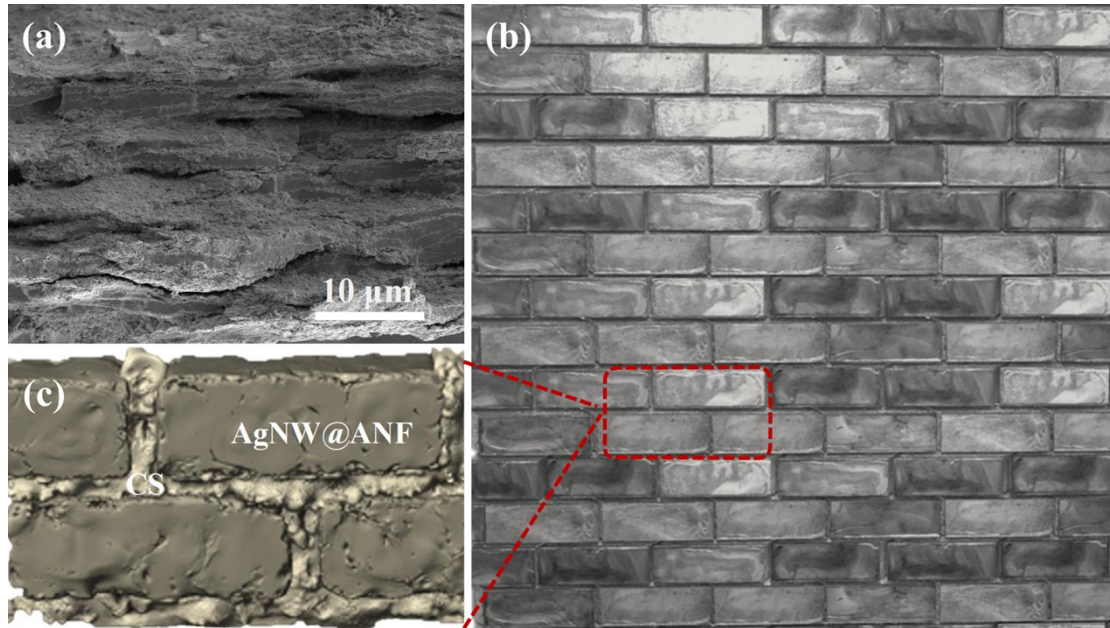
Fig. S25. (a) SEM of AgNW@ANF/CS-CH film, (b-c) Schematic diagram of the brick-mortar structure.
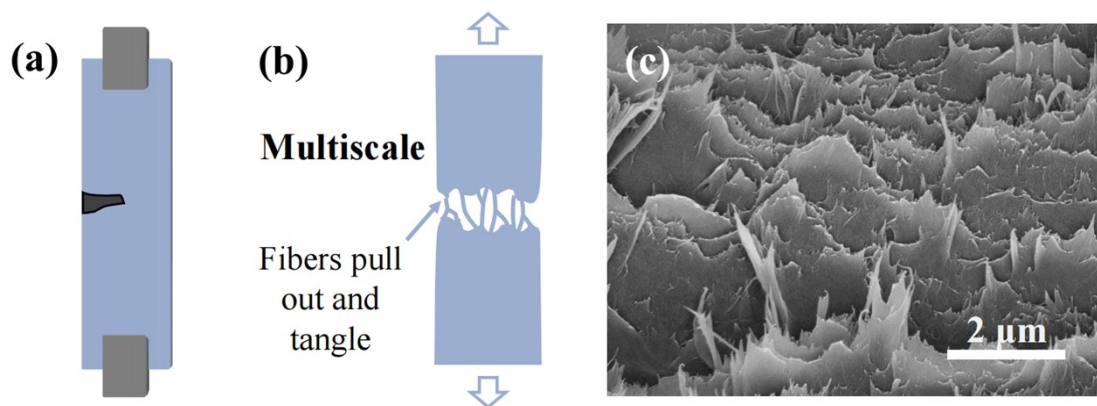
Fig. S26. The (a) tensile and (b) fracture schematics of the film, (c) SEM of the tensile section of the film.

Table S1. Strength and toughness of recently reported ANF-based films [2–11]

No	Sample	Strength (MPa)	Toughness (MJ/m³)	Ref
1	MWCNTs/ANFs	283.5	2.3	1
2	TRGO–ANFs	186.4	3	2
3	ANFs/rHGO/PANI	95.5	4.84	3
4	f-G/ANFs	110	9.9	4
5	rGO/DOPA/BANFs	117	0.61	5
6	RGO/ANFs	100.6	0.37	6
7	MXene/ANFs	160	4	7
8	ANFs/GO	92.89	6	8

9	AgNW/ANFs	285.7	19.8	9
10	ANFs	164.5	10	10
11	AgNW@ANF/CS-CH	306.5	26.5	This work

3.1. DFT calculation

First-principles calculations were carried out using the density functional theory (DFT) method implemented in Gaussian 16W. ANFs and CS were considered two fragments and their energy-optimized geometry was calculated, respectively. AM1 was first used as a semi-empirical method to obtain a general geometry, then hybrid density functional B3LYP and a higher basis set with polarization function and diffusion function were applied to obtain precise energy-optimized geometries. The interaction energy of ANFs (Fregment 1) and CS (Fregment 2) with basis set superposition error correction (BSSE correction) was calculated afterward according to the following equation. The energy of each step indicates the system energy reduction of different distances and conformation of the composite[12].

$$E(interaction) = E_{equilibrium}(ANF/CS) - E(ANF) - E(CS) + E(BSSE) \qquad \textbf{\textit{Eq. S2}}$$

Table S2. Energy in composite film systems

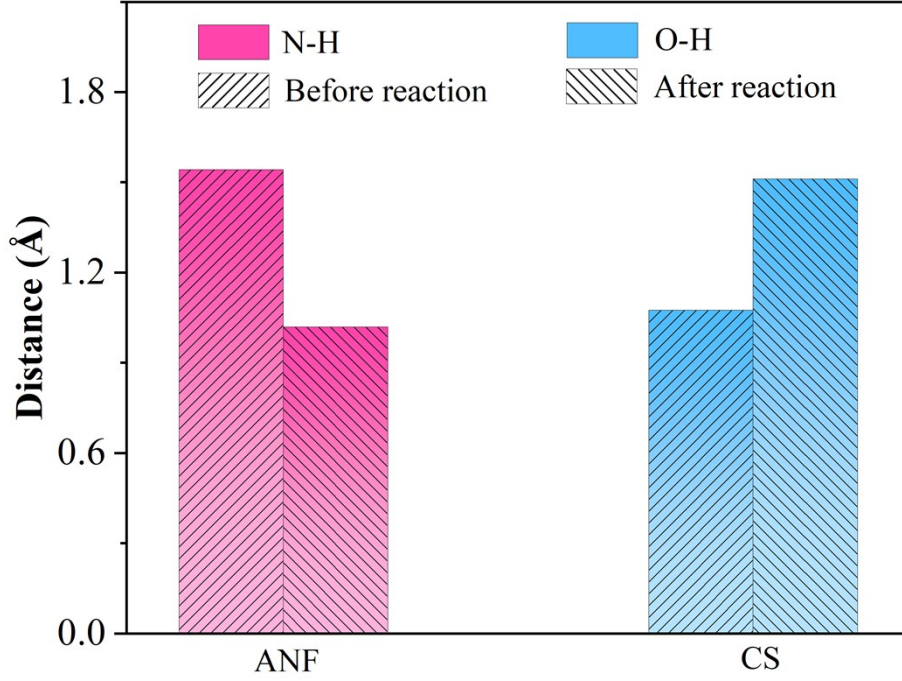| *Samples*	*Interaction*	*ANF/CS*	*ANF*	*CS*	*BSSE*
Energy (eV)	-5.98	-65488.26	-22852.70	-42629.36	0.22

Fig. S27. Change in bond distance simulated by DFT.

4. Electrical performance

4.1. Percolation theory

Percolation models usually serve as the best-known tool for explaining and predicting the electrical properties of conducting filler-based polymer composites. Critical volume fraction, an important parameter in percolation models, is a key parameter to study the electrical properties of these composites at the percolation threshold. Near the percolation threshold, the conductivity of composites experiences a sudden rise in electrical conductivity for several orders of magnitude. These trends in the electrical conductivity of composites near the percolation threshold follow a power law described below:

$$\sigma = \sigma_0(\varphi - \varphi_c)^t \qquad\qquad \textit{Eq. S3}$$

$$\log_{10}\sigma = t \cdot \log_{10}(\varphi - \varphi_c) + \log_{10}\sigma_0 \qquad\qquad \textit{Eq. S4}$$

Where the φ is the weight fraction of the conductive particle in composite material, φ_c is the critical weight fraction of the conductive filler forming a percolation network in the polymer matrix, σ is the electric conductivity of conductive film, σ_0 is

the electric conductivity of conductive filler, and $t$the critical exponent. Substituting *Eq. S5-7* into *Eq. 6*, *Eq. S8* is obtained[13].

$$x = \log_{10}(\varphi - \varphi_c) \qquad \textbf{\textit{Eq. S5}}$$

$$y = \log_{10}\sigma \qquad \textbf{\textit{Eq. S6}}$$

$$b = \log_{10}\sigma_0 \qquad \textbf{\textit{Eq. S7}}$$

$$y = tx + b \qquad \textbf{\textit{Eq. S8}}$$

Table S3. Percolation threshold and critical exponent of conductive films

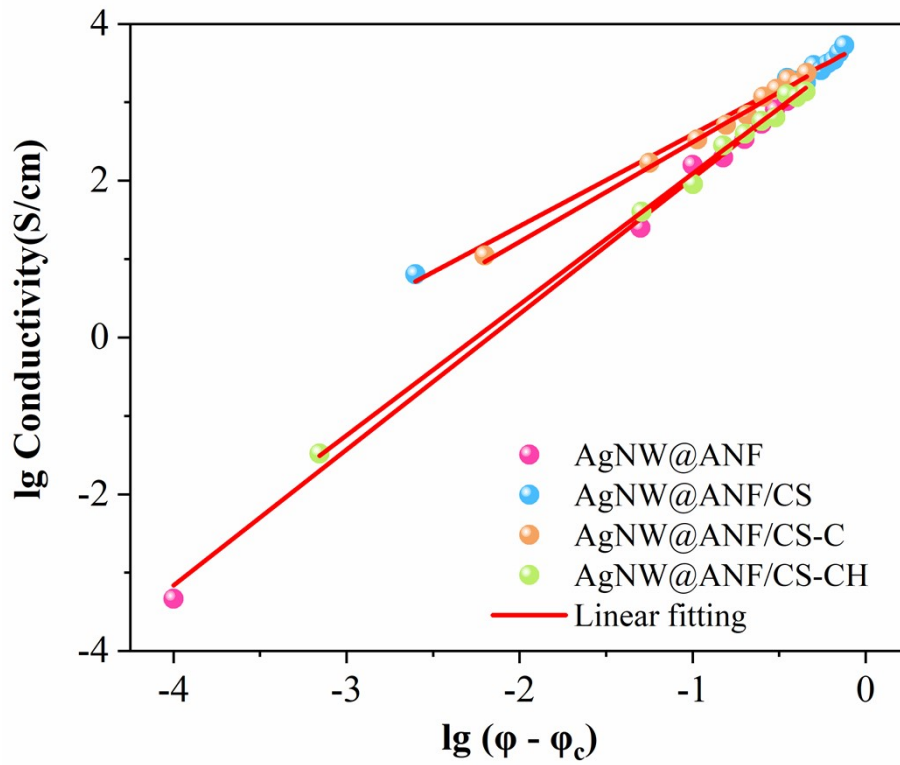| Samples	φ_c	t	R^2
AgNW@ANF	0.59	1.73 ± 0.008	0.984
AgNW@ANF/CSCH	1.35	1.17 ± 0.007	0.993
AgNW@ANF/CS-C	1.09	1.27 ± 0.008	0.989
AgNW@ANF/CS-CH	0.74	1.68 ± 0.009	0.991

Fig. S28. The linear fitting results according to the percolation theory
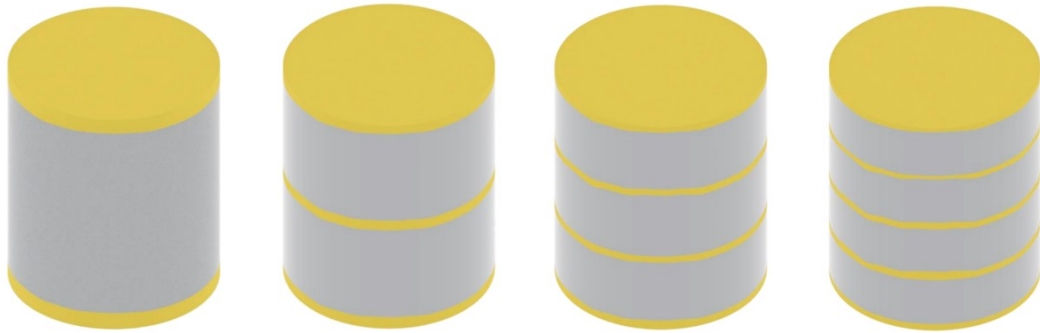
4.2. Comsol simulation

Fig. S29. Schematic diagram of computational simulation models with different layer numbers
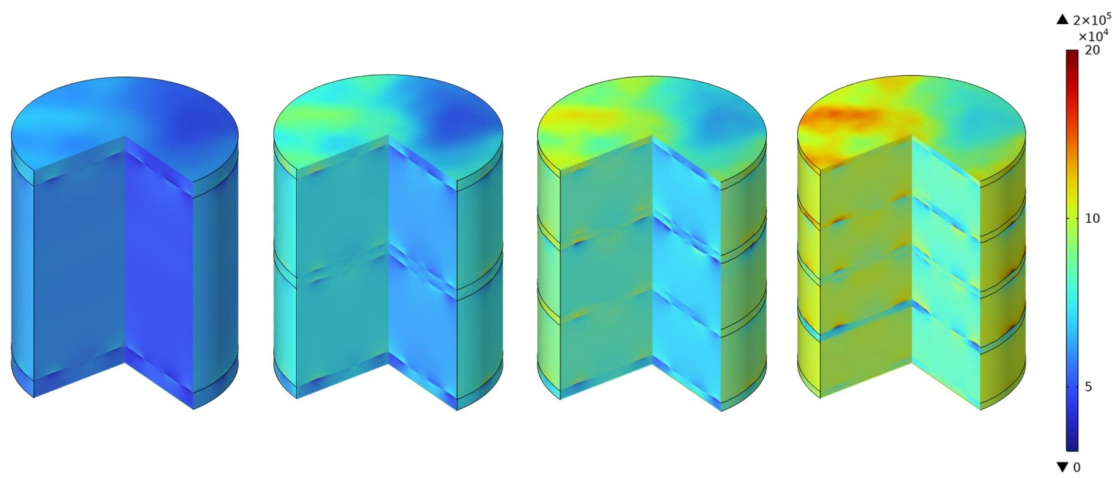
Fig. S30. Simulation results of three-dimensional current density (A/m²) distribution of the above

four models from XYZ-view.

4.3. Hot-pressure sintering
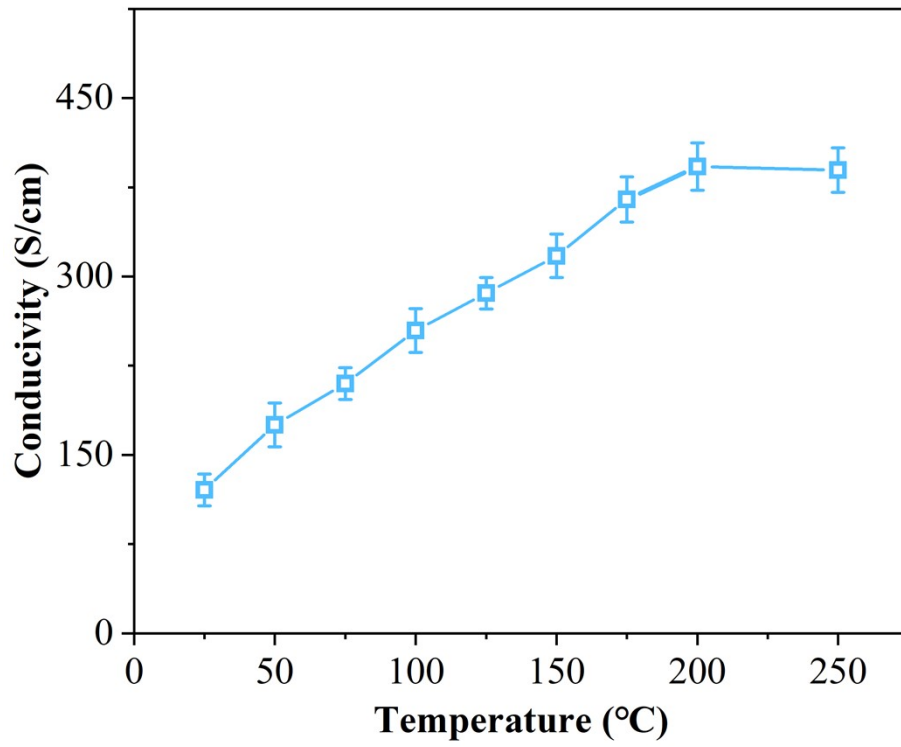
Fig. S31. The conductivity of the films with different temperature

Fig. S32. The conductivity of the films with different pressure

Fig. S33. SEM of AgNWs before and after welding

Fig. S34. The sheet resistance of AgNWs under different hot-pressing sintering temperatures

Fig. S35. The sheet resistance of AgNWs under different hot pressing sintering time

Fig. S36. The sheet resistance of AgNWs under different hot-pressing sintering pressures
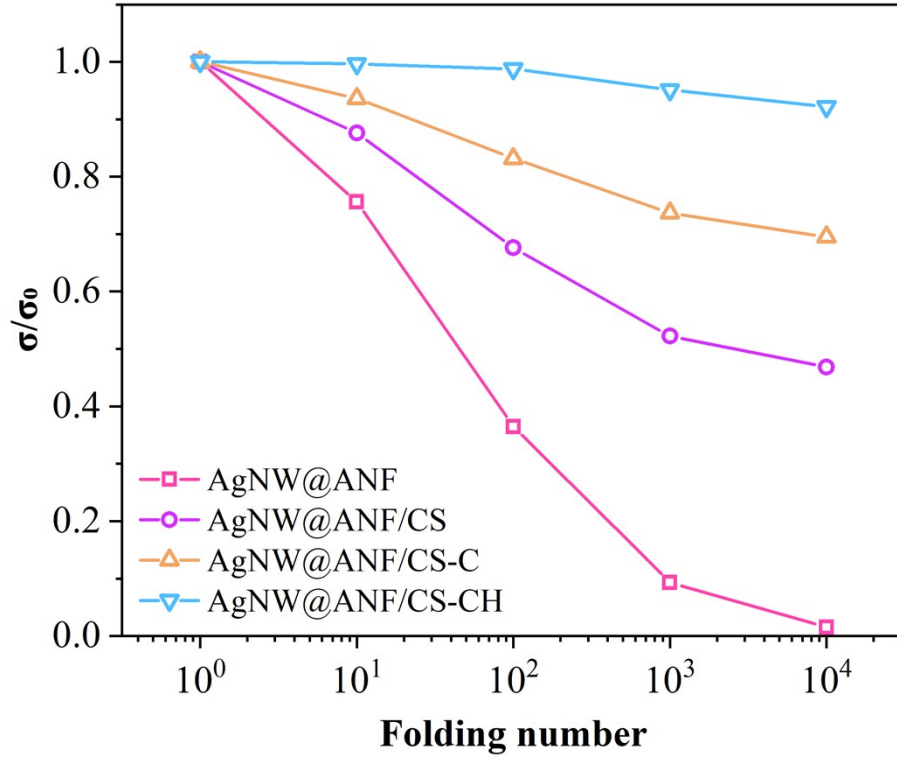
Fig. S37. Conductivity versus initial conductivity under different folding times
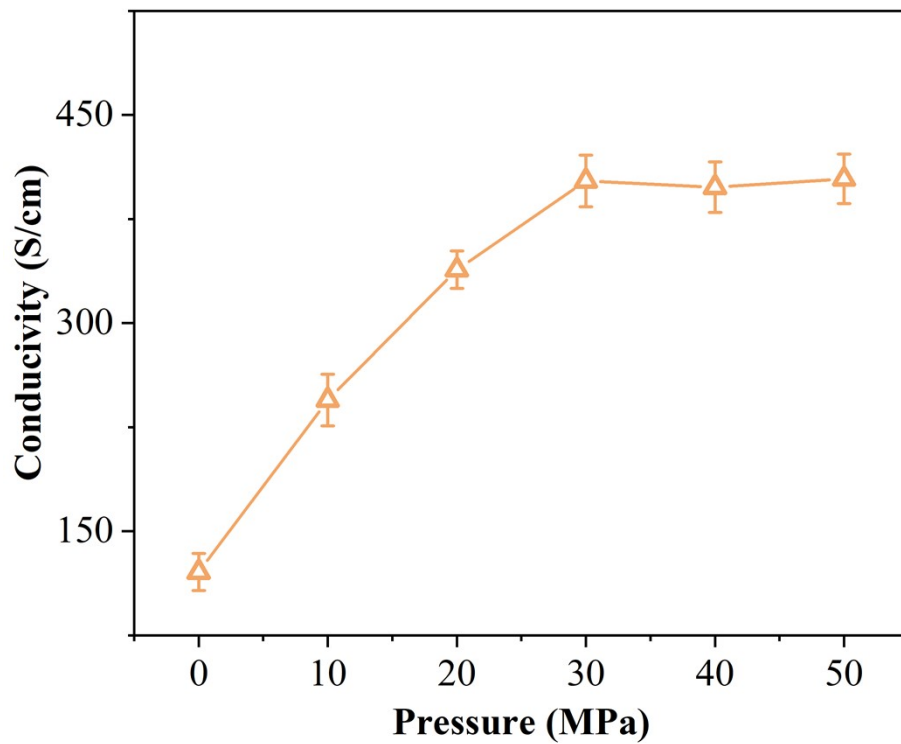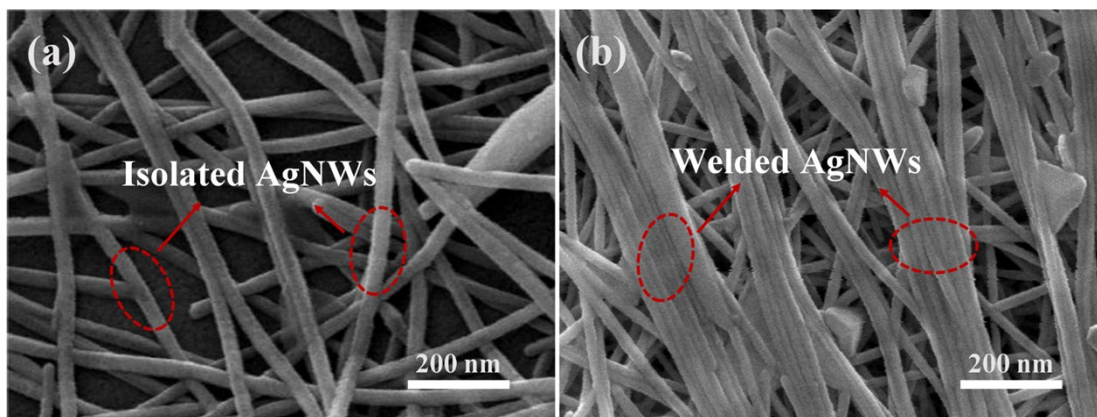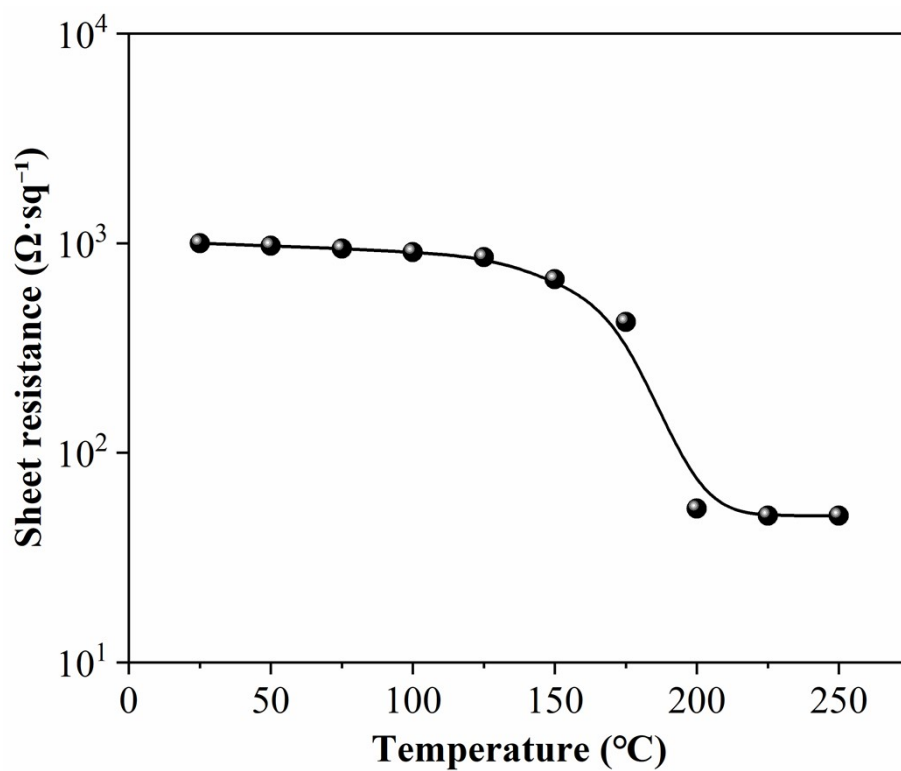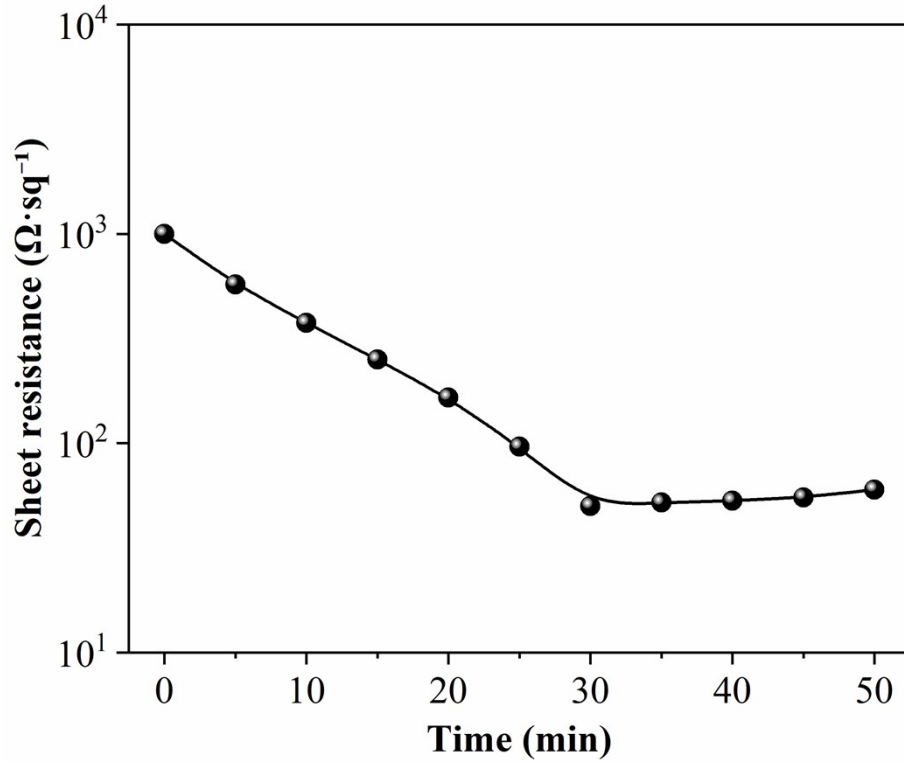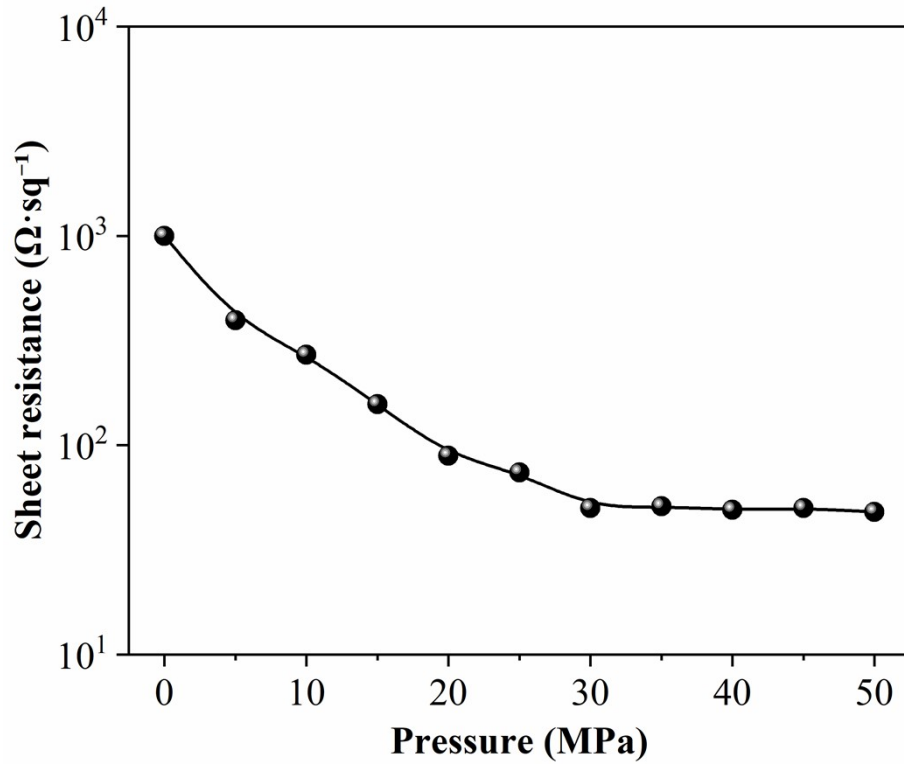
5. EMI Shielding Properties

The EMI shielding effectiveness (SE) of the composites is calculated using S parameters (S11 and S21). The transmission power (T = $|S21|^2$), reflectivity power (R = $|S11|^2$), and absorption power (A) satisfy the equation A + R + T =1[14]. The total EMI shielding effectiveness (SE_T) is equal to the sum of reflection effectiveness (SE_R), and absorption effectiveness (SE_A), which could be described as the following *Eq. S9-S11*:

$$SE_T = SE_A + SE_R \qquad\qquad\qquad\qquad\qquad \textbf{\textit{Eq. S9}}$$

$$SE_A = \left(\frac{|S_{21}|^2}{1 - |S_{11}|^2} \right) \qquad\qquad\qquad\qquad \textbf{\textit{Eq. S10}}$$

$$SE_R = -10\log(1 - R) = -10\log(1 - |S_{11}|^2) \qquad \textbf{\textit{Eq. S11}}$$

The specific shielding effectiveness (SSE) is defined to compare the SE of materials, taking the density into account, and SSE/t is defined in *Eq. S12-13*, taking the thickness into account[15]

$$SSE = \frac{SEM\ SE}{\rho} \qquad\qquad \textit{Eq. S12}$$

$$\frac{SSE}{t} = \frac{SSE}{thickness} \qquad\qquad \textit{Eq. S12}$$

Table S4. SE and SSE/t of recently reported electromagnetic shielding materials [16–25]

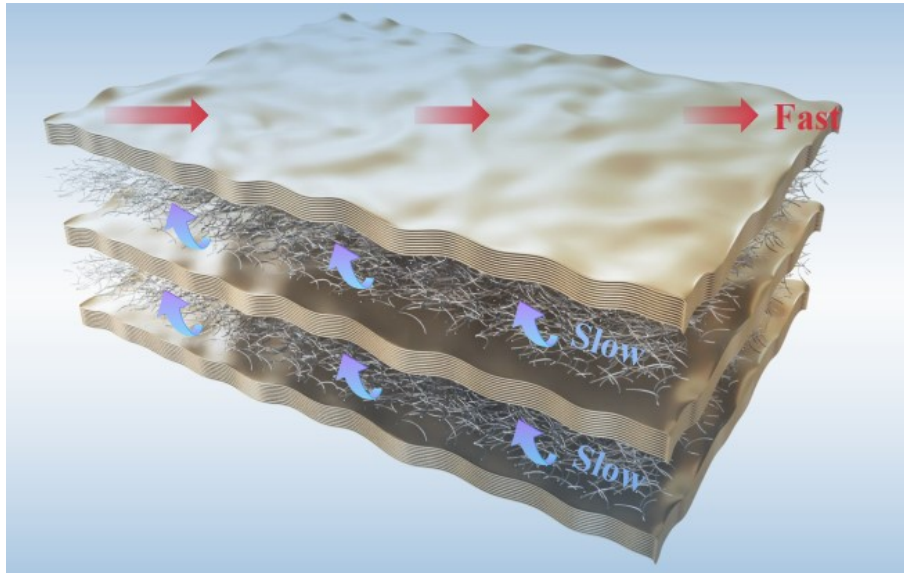| No	Sample	SE (dB)	SSE/t (dB·cm² ·g⁻¹)	Ref
1	CNT/HDPUF	20	8000	11
2	CNT@PU/PU	60	10526.1	12
3	ANF/SWNT	28.5	6000	13
4	PVA/MXene	106	8000	14
5	FC-ANF/CNT	45	11000	15
6	AgNW/PET	37.33	3112.69	16
7	CWF	40	10556	17
8	KM	87.2	10000	18
9	PDMS/AgNWs/TCP	39.1	6600	19
10	PVDF/SiCnw/MXene	38.9	4100	20
11	AgNW@ANF/CS-CH	94.67	22879.1	This work

6. Joule heating

Fig. S38. Anisotropic thermal conduction model of AgNW@ANF/CS-CH film

7. Temperature Sensitivity

AgNWs generate current when electrons move in the direction of an applied electric fie [26,27] ld. AgNWs exhibit irregular thermal motion as the temperature increases, which results in a decrease in directional drift velocity, leading to an increase in resistance. As shown in Fig. S39, when the temperature increases from 25 °C to 150 °C, the film's resistance increases linearly from 293 mΩ to 481 mΩ, which satisfies the positive temperature coefficient. A typical I-V curve for a plastic film is shown in Fig. S40, which illustrates the I-V curve of the film as the temperature increases from 20 to 100 °C, and the current at 0.5 V decreases from 1.7 A at 20 °C to 1.25 A at 100 °C[28–30]. From Fig. S41, the relative resistance change ($\Delta R/R_0$) of the film increases with temperature increase, showing excellent temperature sensitivity (0.5%·°C^{-1}) and linearity (R^2 = 0.98). Furthermore, the $\Delta R/R_0$ decreases during the cooling process, which is in keeping with the curve during heating. Fig. S42 illustrates the $\Delta R/R_0$ curves of the films under different temperature variations, indicating that it is capable of distinguishing temperature differences accurately. As is shown in Fig. S43, the average electrical response remained steady during 400 cycles at $\Delta T = 75$ °C and 35% RH, demonstrating super-high robustness and stability. Fig. S44 illustrates the $\Delta R/R_0$ values of three drops of water placed on the film at three different temperatures (50, 25, and 5 °C). Similarly, the $\Delta R/R_0$ curve shows the opposite trend with water droplets at 50 °C and 5 °C, demonstrating the capability to perceive objects as they are heated. From Fig. S45, the film responds quickly to temperature changes, with a response time of 12.1 s between 25 and 50 ℃.
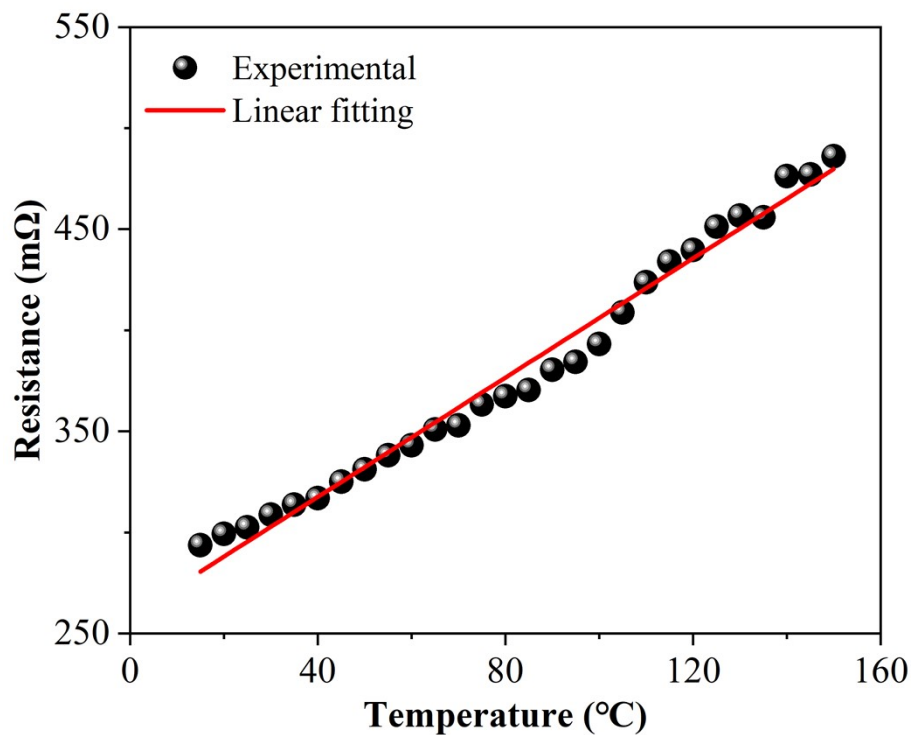
Fig. S39. Resistance-temperature of AgNW@ANF/CS-CH
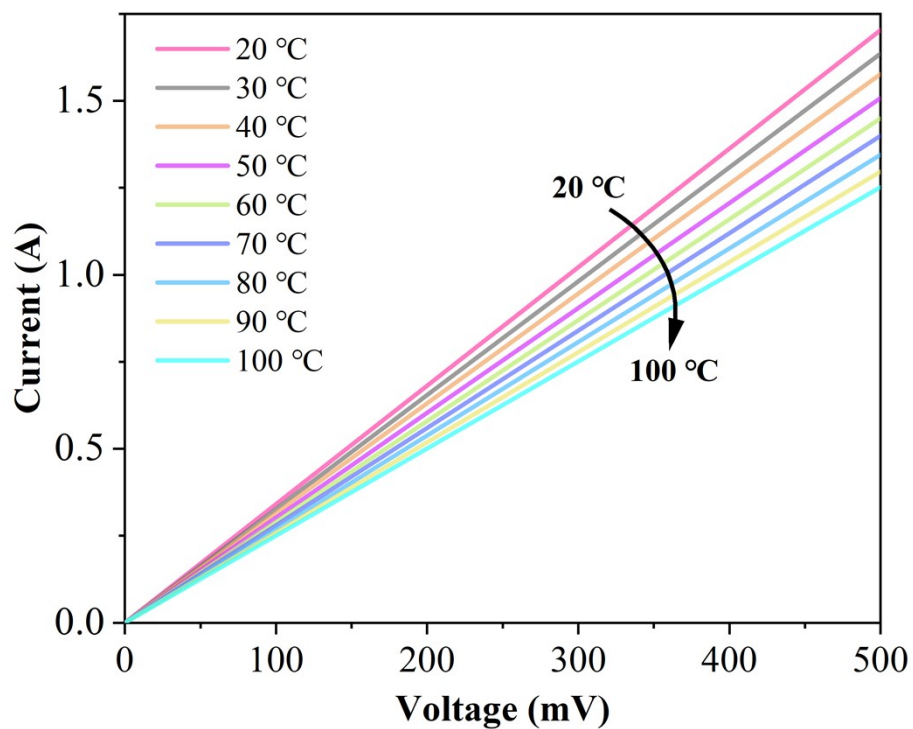

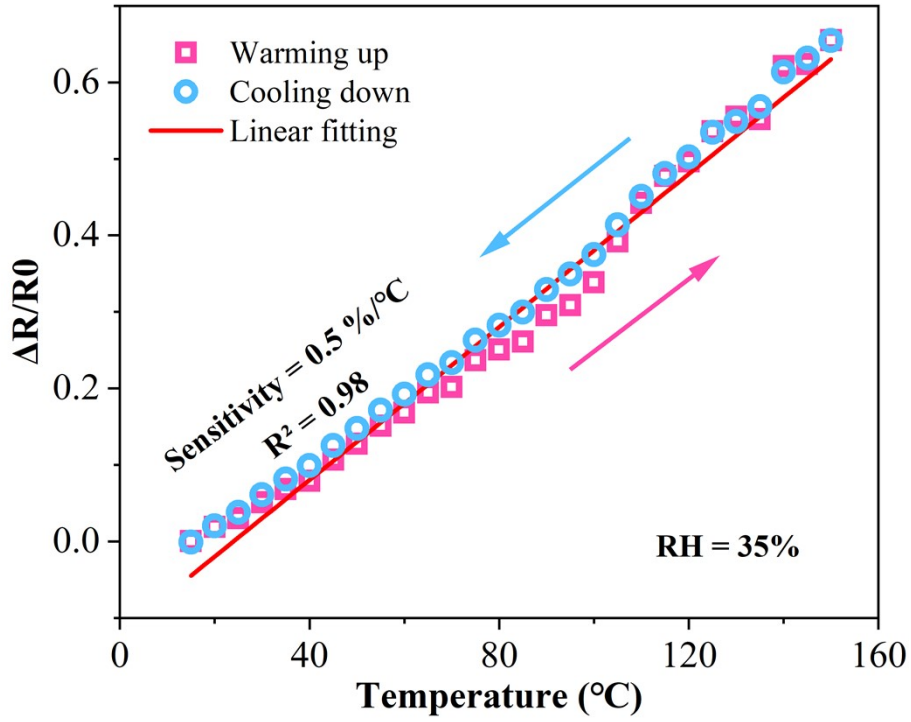**Fig. S40.** The sensitivity-temperature curve of AgNW@ANF/CS-CH

Fig. S41. Curves I–V denote the temperature responses of AgNW@ANF/CS-CH from 20 to

100°C

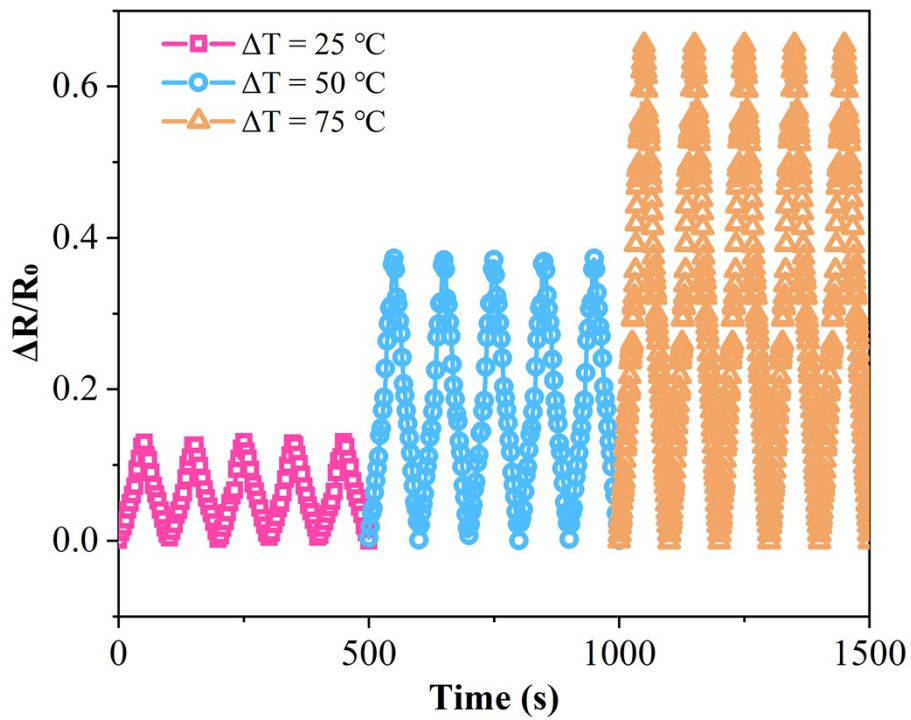**Fig. S42.** Resistance changes at different temperatures

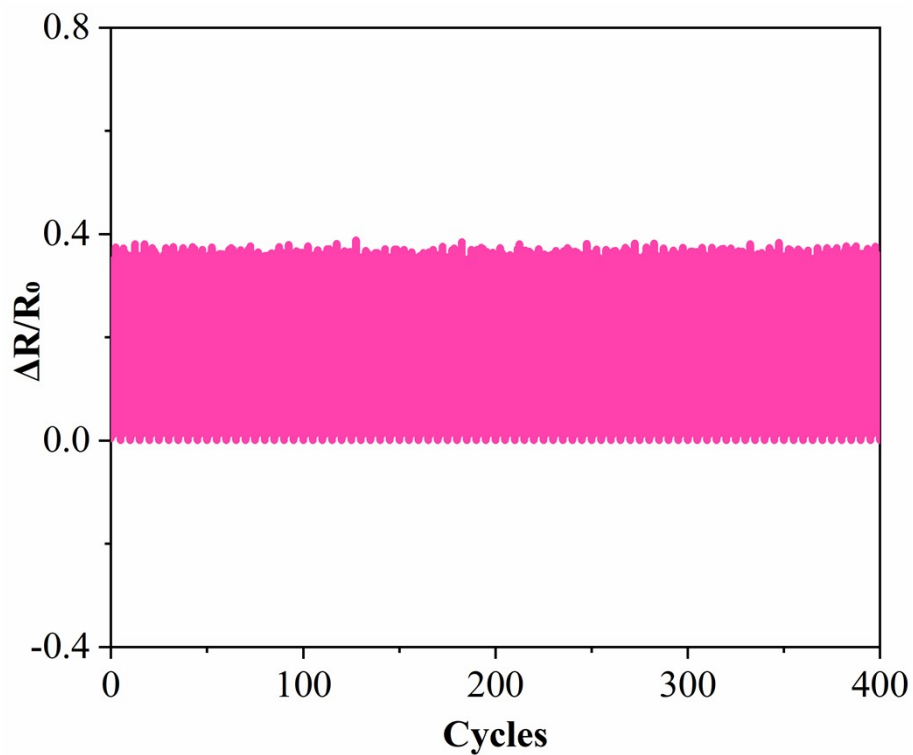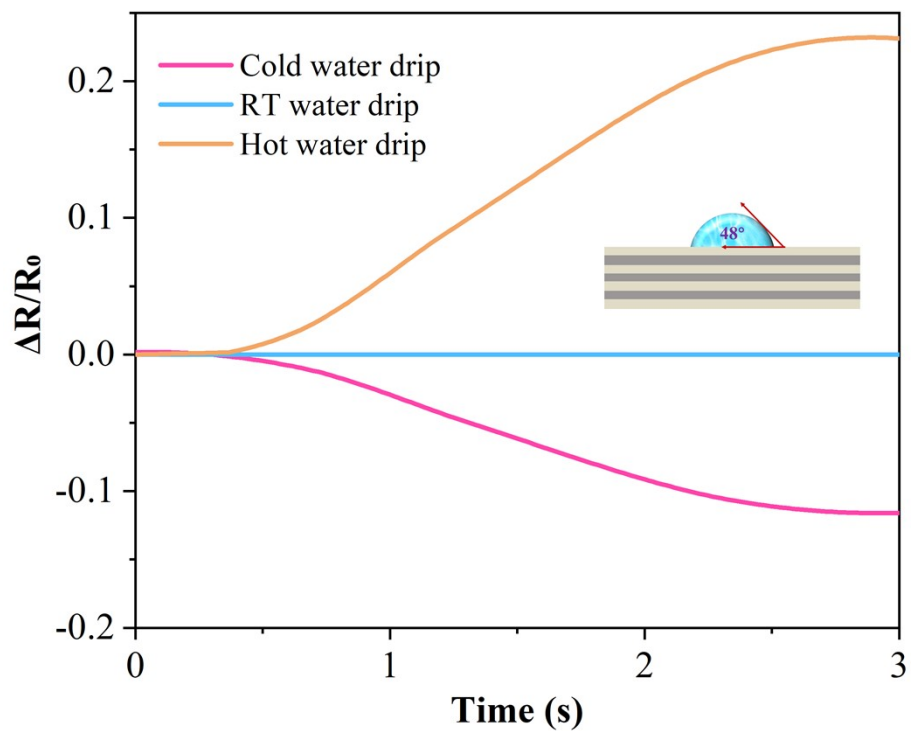**Fig. S43.** The resistance change of the films under 400 cycles (ΔT = 75 °C, 35% RH)

Fig. S44. The resistance change of the films when three drops of water with temperatures of 50 °C (hot), 25 °C (room temperature) and 5 °C (cold)
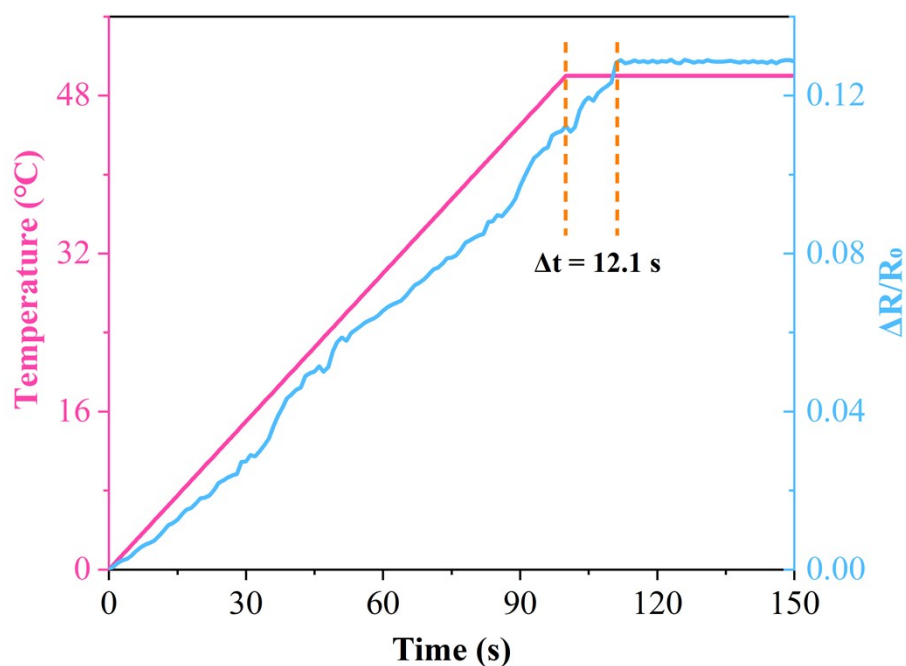
Fig. S45. Relaxation time

Notes and references

1 G. Zhao, X. Cao, Q. Zhang, H. Deng and Q. Fu, *Materials Today Physics*, 2021, **21**, 100483.

2 L. H. Zhao, Y. F. Jin, Z. G. Wang, J. W. Ren, L. C. Jia, D. X. Yan and Z. M. Li, *Ind Eng Chem Res*, 2021, **60**, 8451–8459.

3 B. Yang, W. Li, M. Zhang, L. Wang and X. Ding, *ACS Nano*, 2021, **15**, 7195–7207.

4 J. Chen, W. Xin, W. Chen, X. Zhao, Y. Qian, X. Y. Kong, L. Jiang and L. Wen, *ACS Cent Sci*, 2021, **7**, 1486–1492.

5 B. Yang, L. Wang, M. Zhang, J. Luo and X. Ding, *ACS Nano*, 2019, **13**, 7886–7897.

6 S. R. Kwon, J. Harris, T. Zhou, D. Loufakis, J. G. Boyd and J. L. Lutkenhaus, *ACS Nano*, 2017, **11**, 6682–6690.

7 P. Flouda, S. A. Shah, D. C. Lagoudas, M. J. Green and J. L. Lutkenhaus, *Matter*, 2019, **1**, 1532–1546.

8 J. Zhu, W. Cao, M. Yue, Y. Hou, J. Han and M. Yang, *ACS Nano*, 2015, **9**,

2489–2501.

9   J. Fan, Z. Shi, M. Tian and J. Yin, *RSC Adv*, 2013, **3**, 17664–17667.

10   Z. Zhang, S. Yang, P. Zhang, J. Zhang, G. Chen and X. Feng, *Nat Commun*, 2019, **10**, 1–9.

11   Y. Zou, Z. Chen, Z. Peng, C. Yu and W. Zhong, *Nanoscale*, 2021, **13**, 16734–16747.

12   J. Jin, X.-E. Wu, H. Liang, H. Wang, S. Li, H. Lu, P. Bi, J. Niu, Y. Wu and Y. Zhang, *Mater Horiz*, 2023, **10**, 4626–4634.

13   S. Salaeh, A. Das, K. W. Stöckelhuber and S. Wießner, *Compos Part A Appl Sci Manuf*, 2020, **130**, 105763.

14   Y. Wang, H. K. Peng, T. T. Li, B. C. Shiu, H. T. Ren, X. Zhang, C. W. Lou and J. H. Lin, *Chemical Engineering Journal*, 2021, **412**, 128681.

15   H. Zhang, G. Zhang, Q. Gao, M. Tang, Z. Ma, J. Qin, M. Wang and J. K. Kim, *Chemical Engineering Journal*, 2020, **379**, 122304.

16   G. Zhao, X. Cao, Q. Zhang, H. Deng and Q. Fu, *Materials Today Physics*, 2021, **21**, 100483.

17   X. Zhang, K. Wu, G. Zhao, H. Deng and Q. Fu, *Chemical Engineering Journal*, 2022, **438**, 135659.

18   D. Zhang, W. Song, L. Lv, C. Gao, F. Gao, H. Guo, R. Diao, W. Dai, J. Niu, X. Chen, J. Wei, M. Terrones and Y. Wang, *Carbon*, 2023, **214**, 118315.

19   X. Li, X. Sheng, Y. Fang, X. Hu, S. Gong, M. Sheng, X. Lu and J. Qu, *Adv Funct Mater*, , DOI:10.1002/adfm.202212776.

20   P. Hu, J. Lyu, C. Fu, W. Bin Gong, J. Liao, W. Lu, Y. Chen and X. Zhang, *ACS Nano*, 2020, **14**, 688–697.

21   W. Chen, L. X. Liu, H. Bin Zhang and Z. Z. Yu, *ACS Nano*, 2020, **14**, 16643–16653.

22   X. Ma, J. Pan, H. Guo, J. Wang, C. Zhang, J. Han, Z. Lou, C. Ma, S. Jiang and K. Zhang, *Adv Funct Mater*, 2023, **33**, 202213431.

23   B. Cheng and P. Wu, *ACS Nano*, 2021, **15**, 8676–8685.

24   M. Zhu, X. Yan, X. Li, L. Dai, J. Guo, Y. Lei, Y. Xu and H. Xu, *ACS Appl*

Mater Interfaces, 2022, **14**, 45697–45706.

25   L. Ma, M. Hamidinejad, B. Zhao, C. Liang and C. B. Park, *Nanomicro Lett*, , 2022, **14**, 40820.

26   Q. Hu, G. Ren, J. Ye, B. Zhang, C. Rensing and S. Zhou, *Chemical Engineering Journal*, 2023, **452**, 139169.

27   L. Yang, J. Cui, L. Zhang, X. Xu, X. Chen and D. Sun, *Adv Funct Mater*, 2021, **31**, 1–11.

28   Y. Hou, Z. Sheng, C. Fu, J. Kong and X. Zhang, *Nat Commun*, 2022, **13**, 1–12.

29   G. Ge, Y. Cai, Q. Dong, Y. Zhang, J. Shao, W. Huang and X. Dong, *Nanoscale*, 2018, **10**, 10033–10040.

30   C. Bai, X. Li, X. Cui, X. Yang, X. Zhang, K. Yang, T. Wang and H. Zhang, *Nano Energy*, 2022, **100**, 107449.